# Coastal Trapped Waves: Normal Modes, Evolution Equations, and Topographic Generation

SAMUEL M. KELLY[a] AND SEBASTINE OGBUKA[a]

[a] *Large Lakes Observatory and Physics and Astronomy Department, University of Minnesota Duluth, Duluth, Minnesota*

(Manuscript received 4 October 2021, in final form 9 March 2022)

ABSTRACT: Coastal trapped waves (CTWs) transport energy along coastlines and drive coastal currents and upwelling. CTW modes are nonorthogonal when frequency is treated as the eigenvalue, preventing the separation of modal energy fluxes and quantification of longshore topographic scattering. Here, CTW modes are shown to be orthogonal with respect to energy flux (but not energy) when the longshore wavenumber is the eigenvalue. The modal evolution equation is a simple harmonic oscillator forced by longshore bathymetric variability, where downstream distance is treated like time. The energy equation includes an expression for modal topographic scattering. The eigenvalue problem is carefully discretized to produce numerically orthogonal modes, allowing CTW amplitudes, energy fluxes, and generation to be precisely quantified in numerical simulations. First, a spatially uniform $K_1$ longshore velocity is applied to a continental slope with a Gaussian bump in the coastline. Mode-1 CTW generation increases quadratically with the amplitude of the bump and is maximum when the bump's length of coastline matches the natural wavelength of the CTW mode, as predicted by theory. Next, a realistic $K_1$ barotropic tide is applied to the Oregon coast. The forcing generates mode-1 and mode-2 CTWs with energy fluxes of 6 and 2 MW, respectively, which are much smaller than the 80 MW of $M_2$ internal-tide generation in this region. CTWs also produce 1-cm sea surface displacements along the coast, potentially complicating the interpretation of future satellite altimetry. Prospects and challenges for quantifying the global geography of CTWs are discussed.

KEYWORDS: Coastal flows; Inertia-gravity waves; Internal waves; Kelvin waves; Topographic effects; Waves, oceanic; Tides

## 1. Introduction

Wind and tides generate coastal trapped waves (CTWs) that redistribute energy, create sea surface height (SSH) anomalies, and produce ecologically important coastal currents and upwelling (Mysak 1980; Allen 1980; Brink 1991). CTWs are generated and scatter due to variability in longshore bathymetry and lose energy through small-scale processes (Brink and Allen 1978; Power et al. 1989; Brink 2006) and interactions with mean flows (Narayanan and Webster 1987; Yankovsky and Chapman 1995, 1996). The global energy balance for CTWs, including their role in ocean mixing, is largely unknown (Musgrave 2022). We are unaware of any global power estimates for wind-driven CTWs and have found only one global study on trapped $K_1$ internal tides; Falahat and Nycander (2015) estimated 2 GW of trapped (subinertial) $K_1$ internal-tide generation, much smaller than the 83 GW they estimated for freely propagating $K_1$ tides. Here, we establish a framework for quantifying CTW amplitudes, energy fluxes, and generation that may facilitate further global estimates.

Accurate CTW models are critical for predicting the amplitude and phase of upwelling events and coastal SSH anomalies. The Surface Water Ocean Topography (SWOT) satellite (to be launched in November 2022) will have a 100-km-wide altimeter swath and a 21-day repeat orbit (Carrere et al. 2021). Between each orbit, background stratification and tidal CTW modes can evolve, leading to nonstationary tidal SSH signals that are badly aliased by the orbit and will contaminate observations of mesoscale SSH. Here, we derive evolution equations for CTW modes that may help predict and filter nonstationary tidal CTWs.

*Corresponding author*: Samuel M. Kelly, smkelly@d.umn.edu

The general theory of CTWs unifies the results of numerous piecemeal studies that describe a zoo of waves in various idealized settings [e.g., see the phylogenetic tree in Wang and Mooers (1976)]. Stokes (1846) identified "edge waves" in a nonrotating fluid with a sloping bottom. These waves are trapped by refraction and can propagate in either direction; they are analogous to total internal reflection in optics (LeBlond and Mysak 1978). Thomson (1879) identified "Kelvin waves" in a rotating fluid with a flat bottom and vertical wall. These waves propagate with the coastal wall on their right in the Northern Hemisphere. Robinson (1964) identified "continental shelf waves" in an unstratified, rotating fluid with a sloping bottom. These waves are subinertial, trapped by conservation of relative vorticity, and propagate with the coast on their right in the Northern Hemisphere. Since they have the same restoring force as Rossby waves and can occur on slopes away from coastlines, they are also called barotropic "topographic Rossby waves" (Rhines 1970; Cushman-Roisin and Beckers 2011). Like traditional Rossby waves, continental shelf waves have local maxima in their dispersion curves so that long (short) waves produce energy flux in the direction (opposite direction) of phase propagation. Huthnance (1975) demonstrated that an unstratified, rotating fluid with a sloping bottom and coastal boundary permits (i) a set of superinertial edge waves propagating in both directions, (ii) a Kelvin wave, and (iii) a set of subinertial continental shelf waves that propagate with the coast on their right. Stratification transforms continental shelf waves into CTWs and produces two major modifications: (i) the waves become "bottom-trapped waves" over small slopes (Rhines 1970; Wang and Mooers 1976; Huthnance 1978) and (ii) the dispersion curves monotonically increase, eliminating short

DOI: 10.1175/JPO-D-21-0220.1

waves with energy fluxes in the direction opposite phase propagation (Wang and Mooers 1976; Chapman 1983).

CTW dynamics have often been formulated as an eigenvalue problem with a prescribed longshore wavenumber, pressure eigenvectors, and frequency eigenvalues (Wang and Mooers 1976; Huthnance 1978; Brink 1991). Musgrave (2019) highlights two difficulties with this formulation: (i) each mode is a combination of barotropic and baroclinic motions (see also LeBlond and Mysak 1978), so vertical averaging does not separate large-scale Kelvin waves from shorter CTWs, and (ii) the modes are not orthogonal except in the long-wave (nondispersive) limit (see also Wang and Mooers 1976; Huthnance 1978; Brink 1989), preventing energy fluxes associated with dispersive CTW from being objectively isolated and quantified. This difficulty is circumvented by treating the longshore wavenumber as the eigenvalue (section 2; Webster and Holland 1987; Johnson and Rodney 2011).

Here, we develop and apply a framework for quantifying CTW energy fluxes and generation in realistic settings, with the caveats of neglecting nonlinear effects, mean–flow interactions, and spatially variable inertial frequency. In sections 2a and 2b, we derive the orthogonality relations for CTW modes and present modal evolution and energy equations. In section 2c, we link our results to previous work. The discrete form of the eigenvalue problem is described in section 3a, and general circulation model configurations are described in section 3b. We then quantify CTW generation in simulations of barotropic tidal flow past an idealized coastal bump (section 4a) and on the Oregon coast (section 4b). Section 5 summarizes the results.

## 2. Theory

### a. CTW modes

This study examines small-amplitude perturbations from a quiescent rest state with constant inertial frequency. The restriction to small amplitudes precludes nonlinear processes like wave steepening and eddy formation (Rodney and Johnson 2014). The restriction to a quiescent rest state eliminates interactions between CTWs and mean flows, which have been shown to have major effects on CTW generation, propagation, and dissipation (Narayanan and Webster 1987; Yankovsky and Chapman 1995, 1996). The restriction to constant inertial frequency eliminates the possibility of offshore propagating Rossby waves. The inviscid, unforced, $f$-plane, Boussinesq, hydrostatic equations of motion in Cartesian coordinates are

$$\partial_t u - fv = -\partial_x p, \tag{1a}$$

$$\partial_t v + fu = -\partial_y p, \tag{1b}$$

$$0 = -\partial_z p + b, \tag{1c}$$

$$\partial_t b + wN^2 = 0, \tag{1d}$$

$$\partial_x u + \partial_y v + \partial_z w = 0, \tag{1e}$$

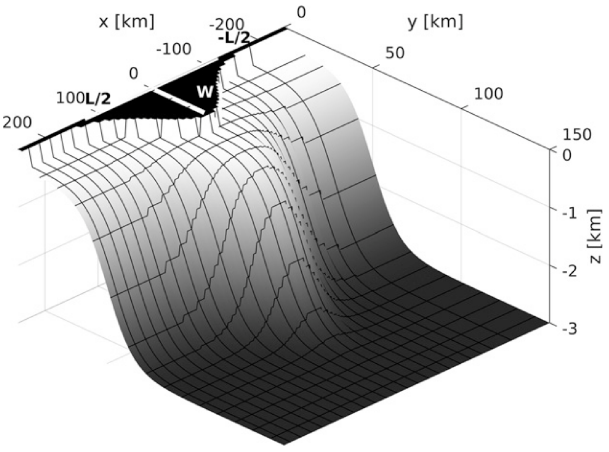


FIG. 1. The idealized-bump bathymetry with annotated axes ($x$, $y$, and $z$) and parameters ($W$ and $L$).

where $x$, $y$, and $z$ are the longshore, cross-shore, and vertical coordinates, respectively (Fig. 1); $u$, $v$, and $w$ are velocities; $p$ is reduced pressure (the perturbation from hydrostatic pressure divided by a reference density $\rho_0$); $b$ is the buoyancy perturbation; and $f$ and $N$ are the inertial and buoyancy frequencies, respectively. An evolution equation for pressure is formed by combining the vertical momentum, buoyancy, and continuity equations (e.g., Kelly 2019)

$$\partial_{tz}\left(\frac{-1}{N^2}\,\partial_z p\right) = -\partial_x u - \partial_y v. \tag{2}$$

The boundary conditions are no-normal flow at the coast, coastal trapping (offshore decay as $y \to \infty$), a linear free surface, and a kinematic flow deflection at the bottom boundary,

$$v = 0 \quad \text{at} \quad y = 0, \tag{3a}$$

$$u, v, p \to 0 \quad \text{as} \quad y \to \infty, \tag{3b}$$

$$\partial_t \eta = w = \frac{-1}{N^2}\,\partial_{zt} p \quad \text{at} \quad z = 0, \tag{3c}$$

$$-v\partial_y H = w = \frac{-1}{N^2}\,\partial_{zt} p \quad \text{at} \quad z = -H, \tag{3d}$$

respectively, where $\eta$ is the surface displacement, $H(x, y)$ is the depth, and the pressure conditions are derived by substituting $b = \partial_z p$ in (1d). The surface boundary condition can be integrated in time to produce $\eta = -\partial_z p/N^2$ at $z = 0$ and the hydrostatic balance yields the useful relation $p = g\eta$ at $z = 0$.

Coastal trapped waves oscillate in $t$ and $x$, so it is useful to Fourier transform the equations of motion and their boundary conditions in one of these dimensions. Historically, the decomposition has been performed in the $x$ direction to yield a known longshore wavenumber, $k$. In this case, the coastal-trapped modes have eigenfrequencies $\omega_n$ and eigenvectors that are nonorthogonal (Wang and Mooers 1976; Brink 1989; Musgrave 2019). Here, we Fourier transform in time to yield a known frequency $\omega$ and

eigenwavenumbers $k_n$. Solving the problem with a known frequency is convenient for narrowband processes, like subinertial tides, but inconvenient for broadband processes, like wind-driven CTWs, because in the latter case the CTW problem must be solved at every frequency in the forcing spectrum. The frequency formulation is also natural for linear scattering problems where the incident wave has a known frequency and only scatters to other modes at that frequency. For a finite length record, $t \in [0, T]$, the Fourier series is

$$u(x,y,z,t) = \sum_{\alpha=-\infty}^{\infty} u_\alpha(x,y,z)\exp(-i\omega_\alpha t), \tag{4}$$

with complex Fourier coefficients

$$u_\alpha(x,y,z) = \frac{1}{T}\int_0^T u(x,y,z,t)\exp(i\omega_\alpha t)dt, \tag{5}$$

with Fourier frequencies $\omega_\alpha = \alpha\pi/T$.

At any frequency of interest, the evolution Eqs. (1a), (1b), and (2), can be written in operator form for a given set of Fourier coefficients $u_\alpha$, $v_\alpha$, and $p_\alpha$:

$$-\mathbf{M}\partial_x\mathbf{x} = -i\mathbf{K}\mathbf{x}, \tag{6}$$

where $\mathbf{x}(x,y,z) = [u_\alpha(x,y,z), iv_\alpha(x,y,z), p_\alpha(x,y,z)]^{\mathrm{T}}$ because $\mathbf{x}$ is a column vector and the operators are

$$\mathbf{M} = \begin{bmatrix} 0 & 0 & 1 \\ 0 & 0 & 0 \\ 1 & 0 & 0 \end{bmatrix} \quad \text{and} \quad \mathbf{K} = \begin{bmatrix} \omega & -f & 0 \\ -f & \omega & -\partial_y \\ 0 & \partial_y & \omega\partial_z\left(\frac{-1}{N^2}\partial_z\right) \end{bmatrix}. \tag{7}$$

The second component of $\mathbf{x}$ is multiplied by $i$ so that the operators are entirely real, which indicates that the across-slope velocity $v$ of a given CTW is in quadrature with the pressure $p$ and alongshore velocity $u$. The vertical boundary conditions for the Fourier coefficients are

$$\eta_\alpha = \frac{-1}{N^2}\partial_z p_\alpha \quad \text{at} \quad z = 0, \tag{8a}$$

$$-v_\alpha\partial_y H = \frac{i\omega}{N^2}\partial_z p_\alpha \quad \text{at} \quad z = -H. \tag{8b}$$

Hereafter, all variables are Fourier coefficients, so we drop the $\alpha$ subscript to simplify notation. Subscripts will instead refer to mode numbers.

Next, we try a solution of the form $\mathbf{x}(x,y,z) = \mathbf{x}_n(y,z)\exp(ik_n x)$ to produce a generalized eigenvalue problem

$$k_n\mathbf{M}\mathbf{x}_n = \mathbf{K}\mathbf{x}_n, \tag{9}$$

where the alongshore wavenumber $k_n$ is the eigenvalue. The eigenvectors (modes, $\mathbf{x}_n$) are orthogonal because $\mathbf{K}$ is self-adjoint (Hermitian) with respect to the inner product

$$\{\mathbf{x}_m, \mathbf{x}_n\} = \int_0^\infty\int_{-H(y)}^0 \mathbf{x}_m^{\mathrm{T}*}\mathbf{x}_n dzdy, \tag{10}$$

where the $^*$ is a complex conjugate. The proof that $\mathbf{K}$ is self-adjoint is illuminating:

$$\begin{aligned}
\{\mathbf{x}_m, \mathbf{K}\mathbf{x}_n\} - \{\mathbf{K}\mathbf{x}_m, \mathbf{x}_n\} &= \int_0^\infty\int_{-H}^0 \left\{u_m^*(\omega u_n - fv_n) - iv_m^*(-fu_n + \omega iv_n - \partial_y p_n) + p_m^*\left[\partial_y iv_n + \omega\partial_z\left(\frac{-\partial_z p_n}{N^2}\right)\right]\right\}dzdy \\
&\quad - \int_0^\infty\int_{-H}^0 \left\{(\omega u_m^* + fv_m^*)u_n + (-fu_m^* - \omega iv_m^* - \partial_y p_m^*)iv_n + \left[-\partial_y iv_m^* + \omega\partial_z\left(\frac{-\partial_z p_m^*}{N^2}\right)\right]p_n\right\}dzdy \\
&= \int_0^\infty\int_{-H}^0 \left[i\partial_y(v_m^* p_n + p_m^* v_n) + \frac{\omega}{N^2}(\partial_z p_m^*\partial_z p_n - \partial_z p_n\partial_z p_m^*)\right]dzdy - \int_0^\infty\left(p_m^*\frac{\omega\partial_z p_n}{N^2} - \frac{\omega\partial_z p_m^*}{N^2}p_n\right)\Big|_{z=-H}^{z=0}dy \\
&= \int_0^\infty i\partial_y\left[\int_{-H}^0 (v_m^* p_n + p_m^* v_n)dz\right]dy - \int_0^\infty i\partial_y H(v_m^* p_n + p_m^* v_n)|_{z=-H}dy \\
&\quad + \int_0^\infty\left[\omega g(\eta_m^*\eta_n - \eta_n\eta_m^*) + i\partial_y H(v_n p_m^* + v_m^* p_n)|_{z=-H}\right]dy \\
&= \left[\int_{-H}^0 (iv_m^* p_n + iv_n p_m^*)dz\right]\Big|_{y=0}^{y=\infty} = 0.
\end{aligned} \tag{11}$$

The Coriolis and kinetic energy terms cancel immediately. In the second equality, integration by parts shows that baroclinic potential energy cancels (recall $\partial_z p_n = b_n$). In the third equality, Liebniz's rule and the fundamental theorem of calculus show that barotropic potential energy cancels and the deflection of cross-shore energy flux at the sloping bottom is

balanced by the vertical energy flux at the bottom. The coastal and offshore boundary conditions on $v_n$ ensure that the final equality is zero, making $\mathbf{K}$ self-adjoint. Note that $\mathbf{K}$ would also be self-adjoint with a rigid-lid boundary condition (i.e., $\partial_z p_n = 0$ at $z = 0$) and/or no-normal flow at an impermeable offshore boundary (e.g., $v_n = 0$ at $y = y_{\max}$).

The modes $\mathbf{x}_n$ are orthogonal because $\mathbf{K}$ is self-adjoint,

$$\{\mathbf{x}_m, \mathbf{K}\mathbf{x}_n\} - \{\mathbf{K}\mathbf{x}_m, \mathbf{x}_n\} = \{\mathbf{x}_m, k_n\mathbf{M}\mathbf{x}_n\} - \{k_m\mathbf{M}\mathbf{x}_m, \mathbf{x}_n\},$$

$$0 = (k_n - k_m)\int_0^\infty \int_{-H}^0 (u_m^* p_n + p_m^* u_n)\,dz\,dy,$$

so that for nondegenerate (unique) eigenvalues and modes with nonzero energy flux, one may normalize $\mathbf{x}_n$ as

$$\rho_0\{\mathbf{M}\mathbf{x}_m, \mathbf{x}_n\} = \rho_0\{\mathbf{x}_m, \mathbf{M}\mathbf{x}_n\} = \rho_0\int_0^\infty \int_{-H}^0 (u_m^* p_n + p_m^* u_n)\,dz\,dy = \delta_{mn}\,(\mathrm{W}), \tag{13}$$

where $\delta_{mn}$ is the Kronecker delta. The $\mathbf{M}$ is a metric tensor that scales the inner product so that it (i) sums quantities with consistent dimensions and (ii) returns the longshore integrated energy flux. The normalization is chosen so that each mode produces 1 W of alongshore energy flux. This normalization follows Brink's (1989) convention that a mode with constant amplitude should conserve longshore energy flux even if parameters such as $f$ and $H$ vary along the coast (see section 2c).

The solution properties of generalized eigenvalue problems are more complicated than those of standard eigenvalue problems. Equation (9) has real and imaginary eigenvalues, which correspond to propagating and evanescent waves. Since $\mathbf{K}$ and $\mathbf{M}$ are self-adjoint, it can be proven that modes with real $k_n$ have nonzero energy flux $\{\mathbf{x}_n, \mathbf{M}\mathbf{x}_n\} \neq 0$ with the same sign as $k_n$ (Parlett 1980). It can also be proven that modes with real $k_n$ can be normalized so that they are entirely real. Thus, $u_n = u_n^*$, $p_n = p_n^*$, and $v_n = -v_n^*$. Solutions with imaginary eigenvalues are nonpropagating (evanescent) and have zero longshore energy flux $\{\mathbf{x}_n, \mathbf{M}\mathbf{x}_n\} = 0$ (see also Webster 1985), so all longshore energy flux must be represented by CTW modes with real $k_n$. Numerical calculations in section 4 support this statement (i.e., 99.99% of energy flux is explained by the first five modes), although we have not derived a completeness theorem.

### b. *Modal evolution and energy equations*

An arbitrary flow with frequency $\omega$ can be written

$$\mathbf{x}(x, y, z)e^{-i\omega t} = \sum_{n=0}^{\infty} \mathbf{x}_n(y, z; x)A_n(x)\exp\left[i(k_n x - \omega t)\right] + \text{residual}, \tag{14}$$

where $k_n$ and $\mathbf{x}_n$ are real, and the "residual" is the component of the flow that produces no longshore energy flux (e.g., a local, evanescent response to a cross-slope obstruction). The temporal oscillation term is superfluous because it appears on both sides of (14), but it is included to emphasize that $A_n$ is a complex harmonic amplitude for waves at the specified Fourier frequency ($\omega$ would be $\omega_\alpha$, had we not dropped the Fourier subscripts).

The semicolon in (14) is used to emphasize that $\mathbf{x}_n$ has a parametric dependence on $x$ because it can be computed for different bathymetric profiles along a coast. At each location, the CTW modes provide an orthogonal basis for the longshore energy flux. When the modes change shape due to a change in the waveguide (coastline), the change of basis "scatters" energy flux from one mode to another. This representation is known as the "reference waveguide method" and has been previously applied to acoustic wave and internal-tide propagation (see, e.g., Lahaye and Llewellyn Smith 2020). The method requires no assumptions about the length scale or smoothness of longshore variability. However, the method can obscure the physical interpretation of CTWs because a CTW amplitude might evolve over a bump not because the underlying waveform changed, but because of changes in the modes used to represent the waveform.

The modal amplitude is

$$A_n(x) = \{\mathbf{x}_n(y, z; x), \mathbf{M}\mathbf{x}(x, y, z)\}/(\mathrm{m}^2\,\mathrm{s}^{-3}), \tag{15}$$

where we must divide by 1 $\mathrm{m}^2\,\mathrm{s}^{-3}$ to make $A_n$ dimensionless because the modes, $\mathbf{x}_n$, and inner product, (10), are dimensional. Projecting (6) onto the $n$th mode yields

$$\{\mathbf{x}_n, \mathbf{M}\partial_x\mathbf{x}\} = \{\mathbf{x}_n, i\mathbf{K}\mathbf{x}\},$$

$$\partial_x\{\mathbf{x}_n, \mathbf{M}\mathbf{x}\} - \{\partial_x\mathbf{x}_n, \mathbf{M}\mathbf{x}\} = i\left\{\mathbf{K}\mathbf{x}_n, \sum_m A_m\mathbf{x}_m + \text{residual}\right\},$$

$$\partial_x A_n - \{\mathbf{M}\partial_x\mathbf{x}_n, \mathbf{x}\} = ik_n\left\{\mathbf{M}\mathbf{x}_n, \sum_m A_m\mathbf{x}_m + \text{residual}\right\},$$

$$\partial_x A_n - ik_n A_n = \{\mathbf{M}\partial_x\mathbf{x}_n, \mathbf{x}\}, \tag{16}$$

where the residual in (14) is orthogonal to $\mathbf{x}_n$ and the modal forcing (i.e., coupling) is $F_n = \{\mathbf{M}\partial_x\mathbf{x}_n, \mathbf{x}\}$. Multiplication of (16) by $(\partial_x + ik_n)$ yields

$$\partial_{xx}A_n + k_n^2 A_n = (\partial_x + ik_n)F_n, \tag{17}$$

the equation for a forced harmonic oscillator. The CTW amplitude evolves downstream the way the angle of a pendulum evolves in time. Longshore bumps act like external forces, so large resonant responses occur where topographic wavenumbers match CTW wavenumbers.

A time-averaged modal energy equation is obtained by multiplying (16) by $\rho_0 A_n^*$ and taking the real part

$$\partial_x F_n = C_n\,(\mathrm{W\,m^{-1}}) \tag{18}$$

where

$$F_n = \frac{1}{2}|A_n|^2\rho_0\{\mathbf{M}\mathbf{x}_n, \mathbf{x}_n\} = \frac{1}{2}|A_n|^2\rho_0\int_0^\infty \int_{-H}^0 (p_n^* u_n + u_n^* p_n)\,dz\,dy\,(\mathrm{W}) \tag{19}$$

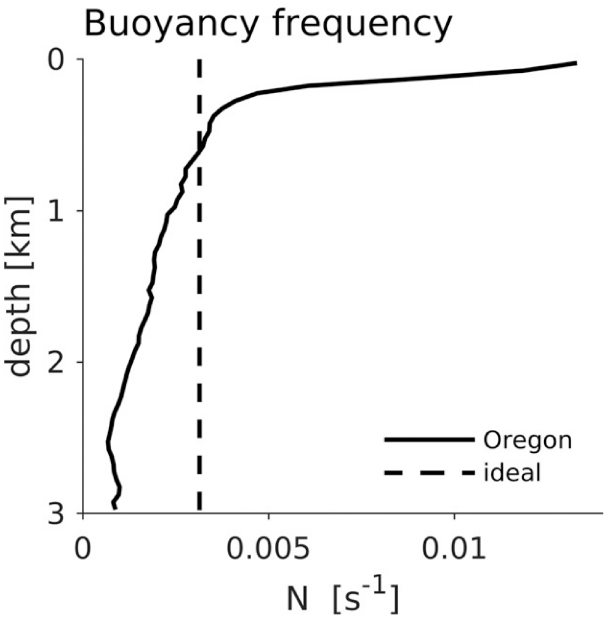


FIG. 2. Oregon and idealized stratification. The vertical mode-1 eigenspeeds (not CTW speeds) are 2.2 and 3 m s$^{-1}$, respectively (Kelly 2016).

is the longshore energy flux in the $n$th mode and the double integral evaluates to 1 W [see (13)]. The expression for intermodal energy transfer due to topographic scattering is

$$C_n = \mathrm{Re}[\rho_0 A_n^* \{\mathbf{M}\partial_x \mathbf{x}_n, \mathbf{x}\}] = \mathrm{Re}\left[\frac{1}{2}\rho_0 A_n^* \int_0^\infty \int_{-H}^0 (u\partial_x p_n^* + p\partial_x u_n^*) dz dy\right], \tag{20}$$

which depends on the total $u$ and $p$ fields and the longshore gradient of the modes $\partial_x \mathbf{x}_n$. While $C_n$ is a generic expression for topographic scattering, we refer to it as to "CTW generation" in this study because we only analyze simulations that generate CTWs from an oscillating barotropic current that approximates a mode-0 Kelvin wave.

Energy transfers between two specific modes could be quantified if $u$ and $p$ in (20) were expanded as a sum of CTWs. Unfortunately, the expansions are incomplete because of the residual in (14), which is not necessarily orthogonal to $\partial_x \mathbf{x}_n$. Physically, the residual is the sum of the evanescent modes, which describe the flow adjustment to a topographic bump that does not project onto CTWs. Yankovsky and Chapman (1995) discuss evanescent modes in numerical simulations and emphasize that they are as relevant for predicting coastal circulation as propagating CTWs (see also simulations by Wilkin and Chapman 1987, 1990).

### c. Connection to previous results

Webster and Holland (1987) and Johnson and Rodney (2011) derived CTW modes from a quadratic eigenvalue problem for pressure with a longshore wavenumber as the eigenvalue. They transformed this problem into a regular eigenvalue problem through several nonobvious substitutions and showed that the modes were orthogonal. Webster and Holland (1987) derived an evolution equation similar to (16) that included wind forcing but not topographic scattering. Our orthogonality condition appears to be equivalent to these previous studies, except that the origin and physical interpretation are more apparent.

Using the procedures in section 2a, it is straightforward to show that the energy operator

$$\mathbf{E} = \frac{1}{2}\begin{bmatrix} 1 & 0 & 0 \\ 0 & 1 & 0 \\ 0 & 0 & \partial_z\left(\frac{-1}{N^2}\partial_z\right) \end{bmatrix} \tag{21}$$

is not self-adjoint

$$\begin{aligned}
\{\mathbf{x}_m, \mathbf{E}\mathbf{x}_n\} - \{\mathbf{E}\mathbf{x}_m, \mathbf{x}_n\} &= \frac{1}{2}\int_0^\infty \int_{-H}^0 \left[u_m^* u_n + v_m^* v_n + p_m^* \partial_z\left(\frac{-\partial_z p_n}{N^2}\right)\right] dz dy \\
&\quad - \frac{1}{2}\int_0^\infty \int_{-H}^0 \left[u_m^* u_n + v_m^* v_n + \partial_z\left(\frac{-\partial_z p_m^*}{N^2}\right) p_n\right] dz dy \\
&= \frac{1}{2}\int_0^\infty \left[\int_{-H}^0 \frac{1}{N^2}(\partial_z p_m^* \partial_z p_n - \partial_z p_m^* \partial_z p_n) dz - \left(p_m^* \frac{\partial_z p_n}{N^2} - \frac{\partial_z p_m^*}{N^2} p_n\right)\Big|_{z=-H}^{z=0}\right] dy \\
&= \frac{1}{2}\int_0^\infty \frac{i}{\omega}(p_m^* w_n + w_m^* p_n)\Big|_{z=-H} dy,
\end{aligned} \tag{22}$$

because when $\partial_y H \neq 0$ the vertical energy flux at the bottom must be balanced by a cross-shore energy flux, which is not included in the energy operator. Since the phase between modes $m$ and $n$ oscillates along the coast, one might try to eliminate the cross term by averaging over the beat distance. In this case, longshore-averaged energy is orthogonal for each mode, as noted by Huthnance (1978). In practice, this averaging is unfeasible because several modes may be present, including

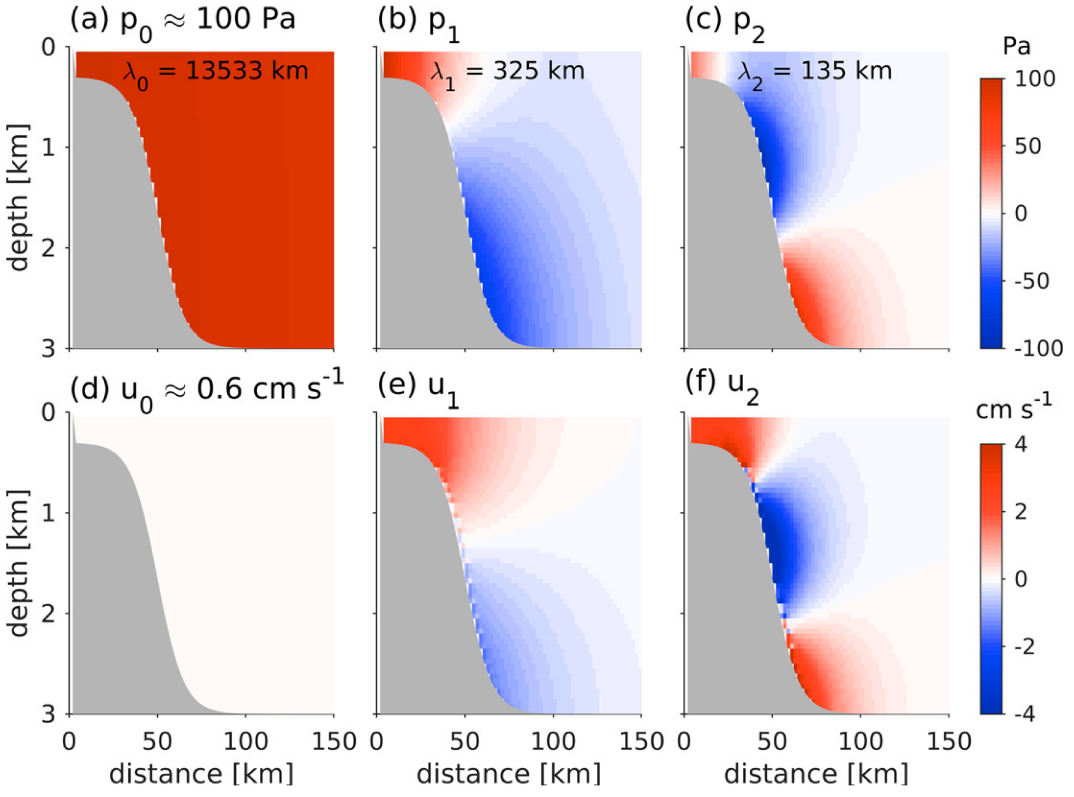


FIG. 3. Pressure, longshore velocity, and wavelengths for CTW modes 0, 1, and 2 in the idealized simulation. For plotting purposes, the modes have been renormalized to produce a 1-cm maximum surface displacement [$\eta = p_n(z = 0)/(\rho_0 g)$]. Mode 0 is approximately constant, and the values are listed.

evanescent modes, making it impossible to define a correct beat distance.

The procedures in section 2a also confirm that the long-wave approximation produces CTWs that are orthogonal even when $\omega$ is treated as the eigenvalue. Assuming $\omega \ll f$, one can neglect the time derivative in (1b) and write the equations of motion

$$\frac{1}{c_n}\mathbf{M}\mathbf{x}_n' = \mathbf{K}'\mathbf{x}_n', \tag{23}$$

where $c_n = \omega/k$ is an eigenspeed, so either $k$ or $\omega$ can be regarded as the eigenvalue. The modified eigenvector is $\mathbf{x}_n' = [u_n, iv_n/\omega, p_n]^{\mathrm{T}}$, where $v_n$ can be recovered after determining $\omega$. The $\mathbf{M}$ operator is defined in (7) and

$$\mathbf{K}' = \begin{bmatrix} 1 & -f & 0 \\ -f & 0 & -\partial_y \\ 0 & \partial_y & \partial_z\left(\dfrac{-1}{N^2}\partial_z\right) \end{bmatrix}, \tag{24}$$

which is self-adjoint, so the modes are orthogonal according to (13), as before.

Previously, orthogonality conditions were derived from a pressure equation and stated in terms of pressure alone (e.g., Wang and Mooers 1976; Brink 1989). The orthogonality condition here can also be stated solely in terms of pressure by expressing longshore velocity in terms of pressure

$$u_n = \frac{f\partial_y p_n - \omega k_n p_n}{f^2 - \omega^2}, \tag{25}$$

and substituting the expression into (13) to produce

$$\int_{-H}^{0}(p_m p_n)|_{y=0} + \int_0^{\infty}\partial_y H(p_m p_n)|_{z=-H}dy + (k_m + k_n)\frac{\omega}{f}\int_0^{\infty}\int_{-H}^{0} p_m p_n dz dy = \left(\frac{\omega^2 - f^2}{f}\right)\delta_{mn}, \tag{26}$$

where Liebniz's rule has been used. The long-wave approximation $u_n = \partial_y p_n/f$, simplifies the orthogonality condition to

$$\int_{-H}^{0}(p_m^* p_n)|_{y=0}\,dz + \int_0^{\infty}\partial_y H(p_m^* p_n)|_{z=-H}dy = -f\delta_{mn}, \tag{27}$$

which is standard in the literature (e.g., Brink 1989) and also consistent with assuming $\omega \ll f$ in (26).

## 3. Numerical methods

### a. The discrete eigenvalue problem

Only $u_n$ and $p_n$ are needed to determine CTW amplitudes and energy fluxes. Using the polarization relations to eliminate $v_n$ reduces the eigenvalue problem (9) to

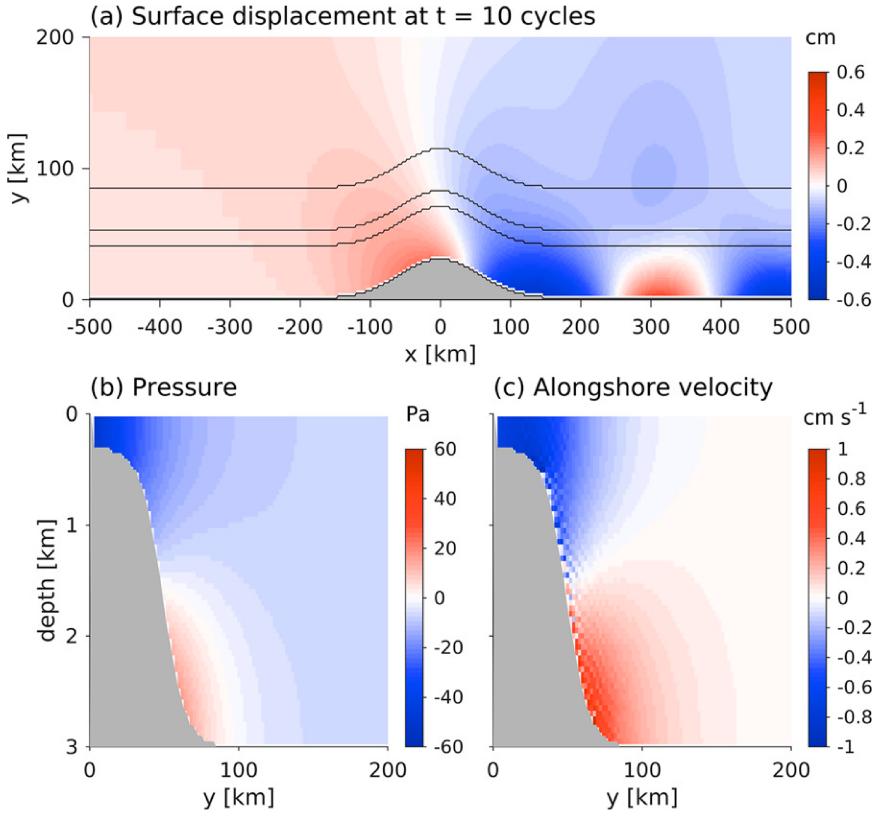


FIG. 4. (a) A snapshot of surface displacement in an MITgcm simulation with a Gaussian coastline bump ($L$ = 250 km and $W$ = 30 km) reveals (i) a large-scale pressure gradient due to barotropic flow around the bump and (ii) the generation of mode-1 CTWs ($\lambda_1$ = 325 km) at the bump, which propagate to the right. The depth-contour interval is 1 km. Cross-shore snapshots of (b) $p$ and (c) $u$ downstream of the bump (at $x$ = 200 km) are consistent with a mode-1 CTW (cf. Fig. 3).

$$\tilde{\mathbf{M}}\tilde{\mathbf{x}}_n = c_n\tilde{\mathbf{K}}\tilde{\mathbf{x}}_n, \tag{28}$$

with $c_n = \omega/k_n$, $\tilde{\mathbf{x}}_n = [u_n, p_n/f]^{\mathrm{T}}$, and operators

$$\tilde{\mathbf{M}} = \begin{bmatrix} 0 & 1 \\ 1 & 0 \end{bmatrix}, \quad \text{and} \tag{29}$$

$$\tilde{\mathbf{K}} = \frac{f}{\omega^2}\begin{bmatrix} \dfrac{\omega^2}{f^2} - 1 & -\partial_y \\ \partial_y & \partial_{yy} + \partial_z\left(\dfrac{-\omega^2}{N^2}\,\partial_z\right) \end{bmatrix}. \tag{30}$$

The results in section 2 still apply to this system, but (28) is easier to solve numerically than (9).

The discretized version of (30) is carefully constructed so that the matrices are self-adjoint and the CTW modes are numerically orthogonal. The $u_n$ and $p_n$ are solved on a staggered C-grid with uniform $\Delta y$ and $\Delta z$. The $u_n$ nodes are placed at the onshore and offshore boundaries of each cell and the $p_n$ nodes are placed in the center. The staggered grid allows the $\partial_y$ operator to be centered in the momentum and pressure equations; however, the staggered grid also requires $u_n$ to be averaged to the center of each cell when computing longshore energy flux. As a result, the identity matrices in (29) are replaced with bidiagonal matrices with values of 1/2.

The boundary condition $v_n = 0$ at the coast is expressed $u_n = \partial_y p_n/f$ using (1b). The continuous problem is self-adjoint in a semi-infinite domain, but our numerical domain requires an offshore boundary condition. The simplest way to code a self-adjoint offshore boundary condition is to specify a vertical wall. This choice permits spurious numerical offshore Kelvin waves. These waves are orthogonal to the CTWs of interest and are easily identified by their negative wave speeds. Both $u_n$ and $p_n$ are specified at the middepth of each cell, so vertical derivatives are calculated using centered differences. This vertical grid naturally allows the specification of free surface or rigid-lid boundary conditions (see Kelly 2016). The bottom is considered locally flat in each grid cell, so the bottom boundary condition is $w_n = 0$, which is equivalent to $\partial_z p_n/f = 0$. Finally, the $u_n(y, z)$ and $p_n(y, z)$ fields are changed from 2D matrices to 1D vectors by listing their values from the coast to the outer wall at each depth, starting at the surface and moving down. The resulting eigenvectors have length $2N_yN_z + N_z$, where the extra $N_z$ accounts for the $u_n$ node at the outer boundary.

The numerical solver is written in MATLAB and searches for waves propagating along the coast and the outer wall,

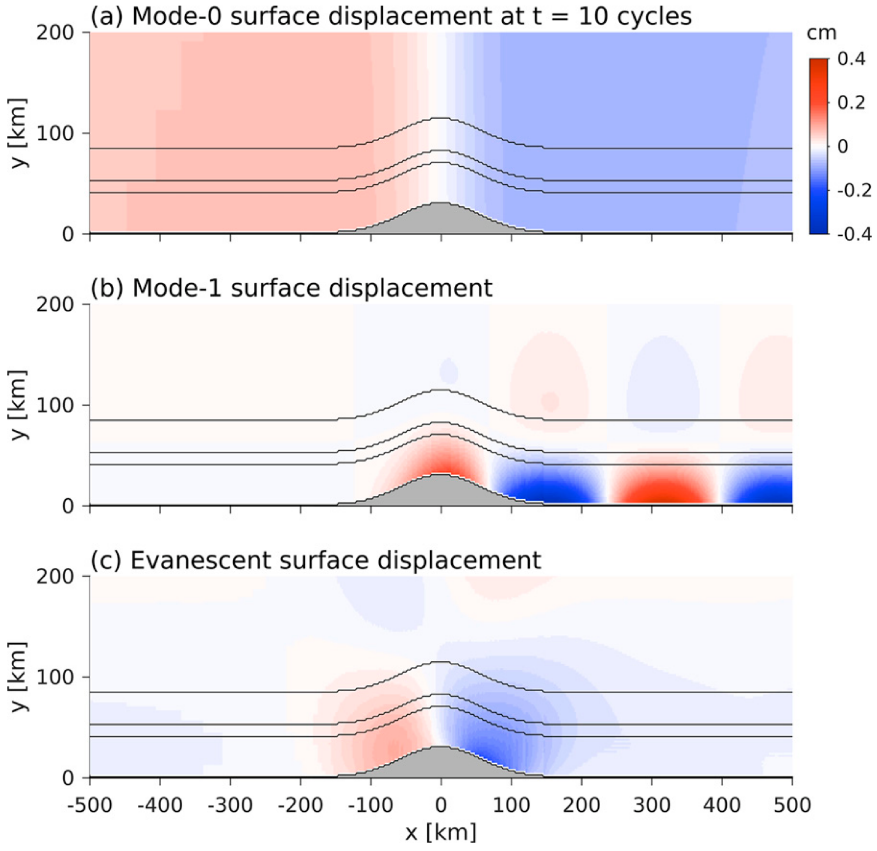


FIG. 5. As in Fig. 4a, but surface displacement is decomposed into mode-0 forcing, which includes (a) both the left- and right-going Kelvin waves, (b) the mode-1 CTW, and (c) the evanescent residual. Surface displacements due to higher-mode CTWs are too small to see on the color scale.

which are distinguished by the sign of $c_n$. The solver finds the fastest waves in both directions, using the shallow water wave speed as a first guess. In practice, the modes are numerically orthogonal so that when $m \neq n$ the discrete version of (13) is on the order of $10^{-10}$.

Johnson and Rodney (2011) present a more sophisticated method for solving the CTW eigenvalue problem with the longshore wavenumber as an eigenvalue. They elegantly solve the numerical problem in a semi-infinite domain using Laguerre functions, which automatically decay offshore. This technique avoids the problem of specifying an artificial offshore boundary. In general, their spectral method is likely more efficient, accurate, and robust than the finite-difference method used here. However, we employ a simple finite-difference method because it can be solved on the native computation grid of our general circulation model simulations, ensuring the modes are numerically orthogonal in the domain of interest.

### b. The general circulation model

The MIT general circulation model (MITgcm; Marshall et al. 1997) is used to simulate CTW generation at idealized coastal bumps and along the Oregon coast. For both types of experiments, grid spacing in the region of interest is 2000 m × 2000 m × 50 m in the $x$, $y$, and $z$ directions, respectively. The idealized simulations have a 16-h inertial period and constant stratification $N = 3\pi/3000$ s$^{-1}$, so that the vertical mode-1 eigenspeed is exactly 3 m s$^{-1}$ for $H = 3$ km, similar to much of the World Ocean (e.g., Rainville and Pinkel 2006). Horizontally uniform stratification on the Oregon slope (Fig. 2) is computed from the *World Ocean Atlas* (*WOA*; Locarnini et al. 2010; Antonov et al. 2010) and has a mode-1 eigenspeed of about 2.2 m s$^{-1}$ (Kelly 2016). The spatially uniform inertial period is 17.4 h, which corresponds to 43.5°N. In both simulations, a $K_1$ (24-h period) barotropic tidal flow generates CTWs as it flows around longshore bumps. We analyze pressure and longshore velocity from each simulation during the 10th tidal cycle, when the CTWs have reached an approximate steady state. Horizontal and vertical numerical viscosities of $10^{-1}$ and $10^{-2}$ m$^2$ s$^{-1}$, respectively, stabilize the model.

The idealized-bump simulations have a high-resolution domain of 600 km × 300 km × 3 km in the longshore, cross-shore, and vertical directions. An additional 100 nodes extend the longshore domain by several thousand kilometers using a telescoping grid that ends with a grid spacing of 2000 km. The domain is periodic in the longshore direction, but CTWs generated by the bump do not reenter the domain of interest in

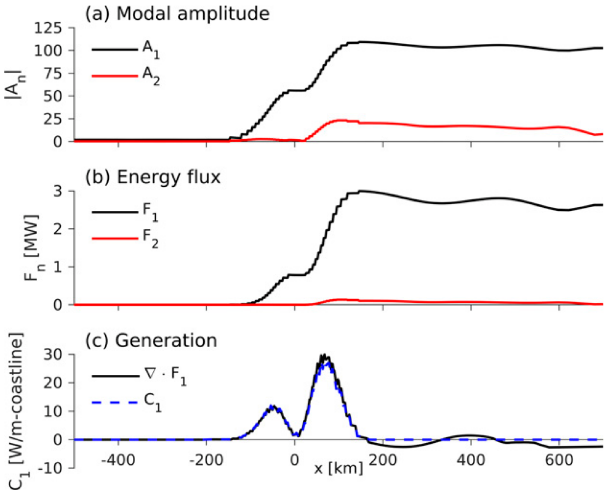


FIG. 6. (a) In the idealized simulation, CTW amplitudes grow over the bump (see Fig. 4) and remain large downstream (to the right). (b) Energy flux increases over the bump before slowly decreasing though numerical dissipation as the waves propagate to the right. Mode-2 energy flux is about 3% of mode-1 energy flux. (c) Mode-1 energy flux divergence is explained by mode-1 generation over the bump.

10 tidal cycles because of the telescoping grid. An oscillating body force generates a spatially uniform 10 cm $s^{-1}$ longshore barotropic current, which projects onto the mode-0 (Kelvin) waves propagating along the coast and offshore boundary. This current subsequently generates CTWs as it flows around a coastal bump. The continental slope bathymetry is

$$H(y) = H_{\text{shelf}} + \frac{H_{\text{abyss}} - H_{\text{shelf}}}{2}\left[1 + \tanh\left(\frac{y - y_{\text{slope}}}{y_{\text{width}}}\right)\right], \quad (31)$$

where $H_{\text{abyss}} = 3$ km is the depth of the abyssal plain, $H_{\text{shelf}} = 300$ m is the shelf depth, and $y_{\text{slope}} = 50$ km is the center of the slope. The width of the slope is $2\pi y_{\text{width}} = 30\pi$ km. The continental slope is shifted to $H(y - y_0)$ to produce a coastal bump, where $y_0$ is a Gaussian curve centered at $x = 0$,

$$y_0(x) = W \exp\left[-\left(\frac{x}{L/\pi}\right)^2\right]. \quad (32)$$

The terms $W$ and $L$ are the amplitude (width) and length of the bump, respectively (Fig. 1). This bathymetry was chosen because the mode shapes are identical everywhere, although shifted offshore, and the Gaussian coastline is compact in both position and wavenumber space (i.e., the Fourier transform of a Gaussian is another Gaussian).

The Oregon domain extends from 124° to 127.5°W and from 41° to 46°N, roughly the region studied by Osborne et al. (2014). The simulation uses realistic bathymetry (Smith and Sandwell 1997) at the coast but has a perfectly flat 3-km abyssal plain to eliminate "noise" due to bottom-trapped modes at small offshore seamounts. Barotropic $K_1$ velocities from the TPXO8.0 atlas (Egbert 1997) force the simulation at the north and south boundaries. A 50-km sponge at the north and south boundaries attenuates any radiating waves. To ensure the numerical CTW modes exactly correspond to the simulation, the offshore boundary is treated as a vertical wall. Excluding forcing at the offshore boundary slightly reduces the accuracy of the barotropic $K_1$ tides in the simulation but does not qualitatively alter the generation of CTWs (not shown). Importantly, the vertical wall at the offshore boundary ensures that the Kelvin wave forcing can be accurately removed because it is numerically orthogonal to the CTW modes.

After completing the simulations, $u$ and $p$ are Fourier transformed in time to obtain the $K_1$ (diurnal) Fourier coefficients. Then we solve (28) on the exact/native MITgcm grid to obtain a set of numerically orthogonal CTW modes. The modal amplitudes and energy fluxes are determined by (15) and (19). CTW generation (20) is approximated

$$\begin{aligned} C_n &\approx \text{Re}\left\{\frac{\rho_0}{2}\left(\frac{A_n^{*+} + A_n^{*-}}{2}\right)\int_0^{\infty}\int_{-H}^{0}\left(u\,\frac{p_n^+ - p_n^-}{\Delta x} + p\,\frac{u_n^+ + u_n^-}{\Delta x}\right)dz\,dy\right\} \\ &\approx \text{Re}\left\{\frac{\rho_0}{4\Delta x}(A_n^{*+} + A_n^{*-})\int_0^{\infty}\int_{-H}^{0}\left[(up_n^+ + pu_n^+) - (up_n^- + pu_n^-)\right]dz\,dy\right\} \\ &\approx \text{Re}\left\{\frac{\rho_0}{4\Delta x}(A_n^{*+} + A_n^{*-})(A_n^+ - A_n^-)\right\} \\ &\approx \rho_0\frac{|A_n^+|^2 - |A_n^-|^2}{4\Delta x}, \end{aligned} \quad (33)$$

where $u$ and $p$ are evaluated at the face of each cell (i.e., the $u$ nodes on the C grid) and the plus and minus superscripts are values at the centers of the adjacent cells (i.e., the $p$ nodes on the MITgcm C grid). The generation term can be interpreted as the difference in modal energy flux when $u$ and $p$ are projected onto the CTW modes to the left and right of each cell face.

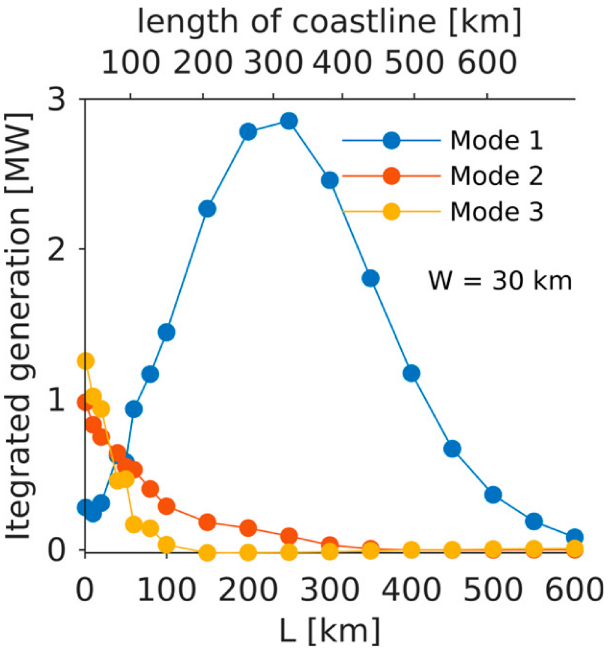


FIG. 7. When $W = 30$ km, mode-1 integrated CTW generation peaks for a bump with $L = 250$ km and a coastline length equal to the mode-1 wavelength ($\lambda_1 = 325$ km). Mode-2 and mode-3 integrated CTW generation are maximum at the narrowest bump, which is a one-grid-cell-wide knife barrier in the simulation.

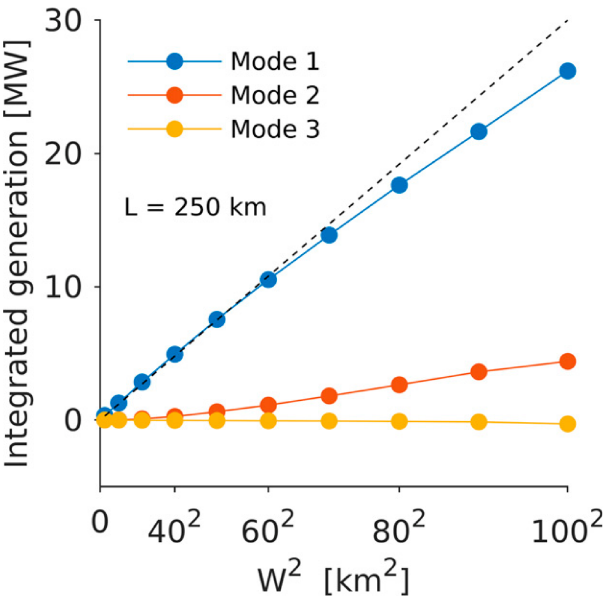


FIG. 8. When $L = 250$ km, mode-1 integrated CTW generation increases quadratically with $W$ (linearly with $W^2$). For reference, the dashed line has a slope of 0.3 (MW km$^{-2}$).

Since both sets of modes resolve the net energy flux, total generation is zero (i.e., $\sum_{n=0}^{\infty} C_n = 0$) and topographic scattering only redistributes energy between modes.

## 4. Applications

### a. Generation by a Gaussian bump

The first three CTW modes over the idealized continental slope (31) have wavelengths of 13 533, 325, and 135 km. Mode 0 is a Kelvin wave that is nearly barotropic, and modes 1 and 2 are labeled by the number of zeros in $p_n$ and $u_n$ (Fig. 3). Both modes 1 and 2 have significant barotropic components on the shelf, but are more baroclinic over the slope. Modes 1 and 2 are strongly influenced by the combined effects of rotation, stratification, and bottom slope.

The oscillating longshore velocity past a coastal bump with $L = 250$ km generates mode-1 CTWs ($\lambda_1 = 325$ km) that propagate with the coast on their right (Fig. 4). These results are qualitatively similar to the subinertial simulations presented by Dale et al. (2001). Projecting the flow onto modes explains 99.99% of the total energy flux and separates the prescribed forcing from the locally generated CTWs and evanescent residual (Fig. 5). The evanescent residual differs from the propagating waves because it is localized around the bump and has a zero contour that is tilted with respect to the coastline and isobaths. The longshore velocity forcing projects onto both left and right going mode-0 waves (the left going wave travels along the offshore wall), which have individual energy fluxes of ±1500 MW, but mostly cancel to produce a net energy flux of −100 MW. The mode-1 and mode-2 amplitudes grow over the bump and remain large toward positive $x$ (to the right; Fig. 6a). The real and imaginary parts of the mode-1 and mode-2 amplitudes (not shown) oscillate with wavelengths of $\lambda_1 = 325$ km and $\lambda_2 = 135$ km, respectively, as predicted by theory. The mode-1 and mode-2 energy fluxes are about 3 MW and 0.1 MW, respectively (Fig. 6b). Unexplained (residual) energy flux is about 0.1 MW at the bump and 0.01 MW away from the bump. The mode-1 flux divergence is almost perfectly balanced by generation over the bump (33), with peak values of about 30 W m$^{-1}$ coastline (Fig. 6c). The accuracy and precision of the modal decomposition in this simulation suggests that the CTWs produced by the MITgcm are consistent with the theory presented in section 2.

When $W = 30$ km, mode-1 longshore-integrated CTW generation is maximum for Gaussian bumps with $L = 250$ km (Fig. 7). One might expect maximum integrated CTW generation when $L$ equals the resonant wavelength ($\lambda_1 = 325$ km) because the downstream evolution of $A_n$ is described by a simple-harmonic oscillator (16). However, the resonance condition is better predicted by the bump's length of coastline, which is equal to 322 km when $L = 250$ km (Fig. 7). Modes 2 and 3 do not indicate a resonant peak when the length of coastline is near their wavelengths, $\lambda_2 = 135$ km and $\lambda_3 = 82$ km. Instead, they are maximum when the bump is narrowest (i.e., a knife-edge barrier in the simulation). We did not investigate the lack of mode-2 and mode-3 resonance, but a plausible explanation is that the prescribed currents primarily produce mode-1 vertical displacements as they flow around the idealized bump. We hypothesize that mode-2 or mode-3 resonance requires a more complicated slope and bump.

When $L = 250$ km, the integrated CTW generation increases quadratically with $W$ (Fig. 8), indicating that $A_n$ increases linearly

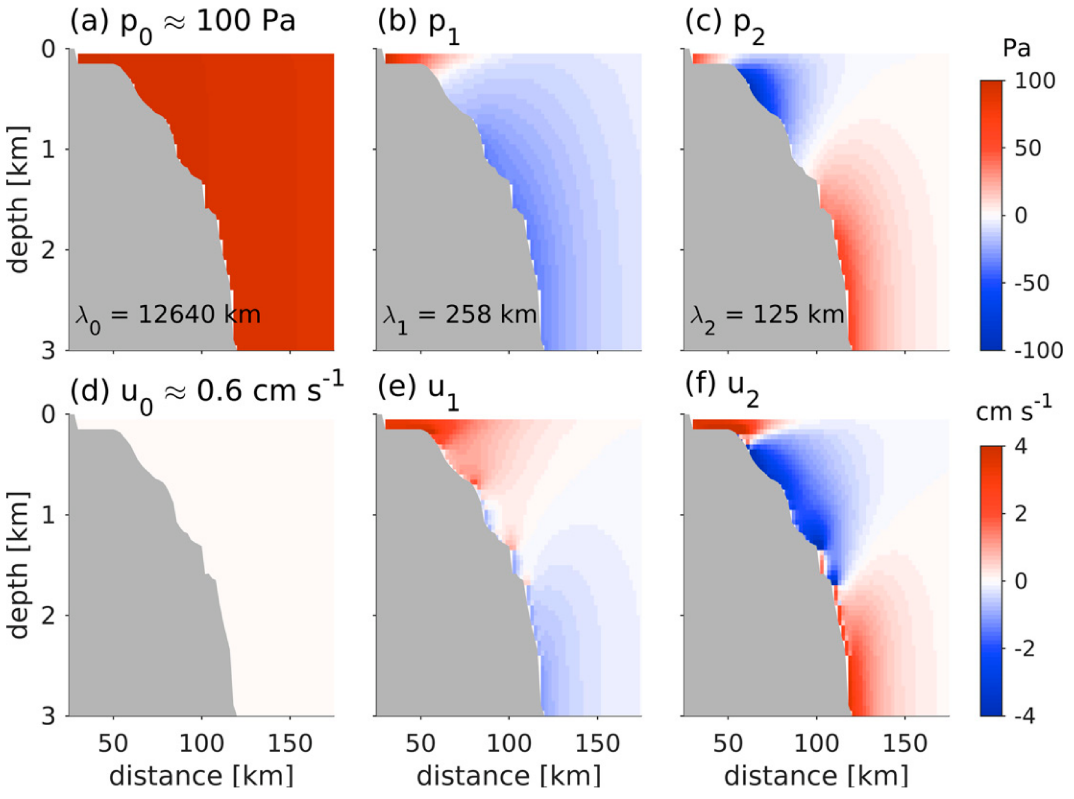


FIG. 9. As in Fig. 3, but for Oregon bathymetry and stratification at 43.5°N.

with $W$. The linear dependence of $A_n$ is predictable from (16) because the forcing is linearly related to $\partial_x \mathbf{x}_n$, which is linearly related to $W$, at least for small changes in $W$. The slower increase in mode-1 generation at large $W$ can be explained by the increased length of coastline, which reduces resonance in (16).

### b. *Generation on the Oregon coast*

CTW modes on the Oregon coast resemble those of the idealized simulations, except they have slightly shorter wavelengths (Fig. 9). The amplitude of the longshore $K_1$ barotropic current in the Oregon coast simulation is similar to that of TPXO8.0 (Figs. 10a,b) and the simulations presented by Osborne et al. (2014). We also find that CTWs contribute to the longshore barotropic current on the shelf at 43.5°N (Fig. 10c), as predicted by Osborne et al.'s (2014) analysis of CTW dispersion relations. Note that modes 1–3 have a larger velocity amplitude than the total velocity because modes 1–3 are out of phase with mode 0, so they interfere destructively. The energetic CTWs also produce a 1 cm surface displacement along the coast, which may complicate coastal estimates of SSH obtained from the upcoming SWOT altimeter.

The mode-1 CTW amplitude is generally larger than the mode-2 amplitude (Fig. 11a), so that mode-1 energy flux is 3–8 MW and mode-2 energy flux is 0–4 MW (Fig. 11b). There are few published estimates of CTW energy fluxes, but Crawford (1984) observed a 50 MW continental shelf wave offshore of Vancouver Island at 49°N. Although the comparison is inexact, these studies suggest $\mathcal{O}(1-100)$ MW $K_1$ CTW energy fluxes in the eastern North Pacific.

Mode-1 and -2 CTW generation on the Oregon coast is around 100 W m$^{-1}$ coastline and exhibits both positive and negative generation regions with no obvious hotspots (Fig. 11c). Like any forced harmonic oscillator, instantaneous power may be positive or negative depending on whether the forcing is in or out of phase with the oscillator, so averaging is required to identify net energy transfer. The largely offsetting regions of positive and negative generation near 42.5°N may be associated with a coastal bump that is much shorter than the CTW wavelengths ($\lambda_1 = 258$ km and $\lambda_2 = 125$ km).

## 5. Summary

CTW modes are orthogonal according to (13) when the longshore wavenumber is treated as the eigenvalue. A similar orthogonality condition was derived by Webster and Holland (1987) and Johnson and Rodney (2011). In contrast, most previous studies have treated frequency as the eigenvalue and derived nonorthogonal modes (e.g., Wang and Mooers 1976; Huthnance 1978; Brink 1989). In the long-wave limit, CTW modes are orthogonal when either wavenumber or frequency is the eigenvalue (section 2c). In all cases, the orthogonal quantity is the local longshore energy flux, not energy.

Projecting the equations of motion (1) onto the $n$th CTW mode yields the modal amplitude evolution equation (16), which is a forced harmonic oscillator where downstream

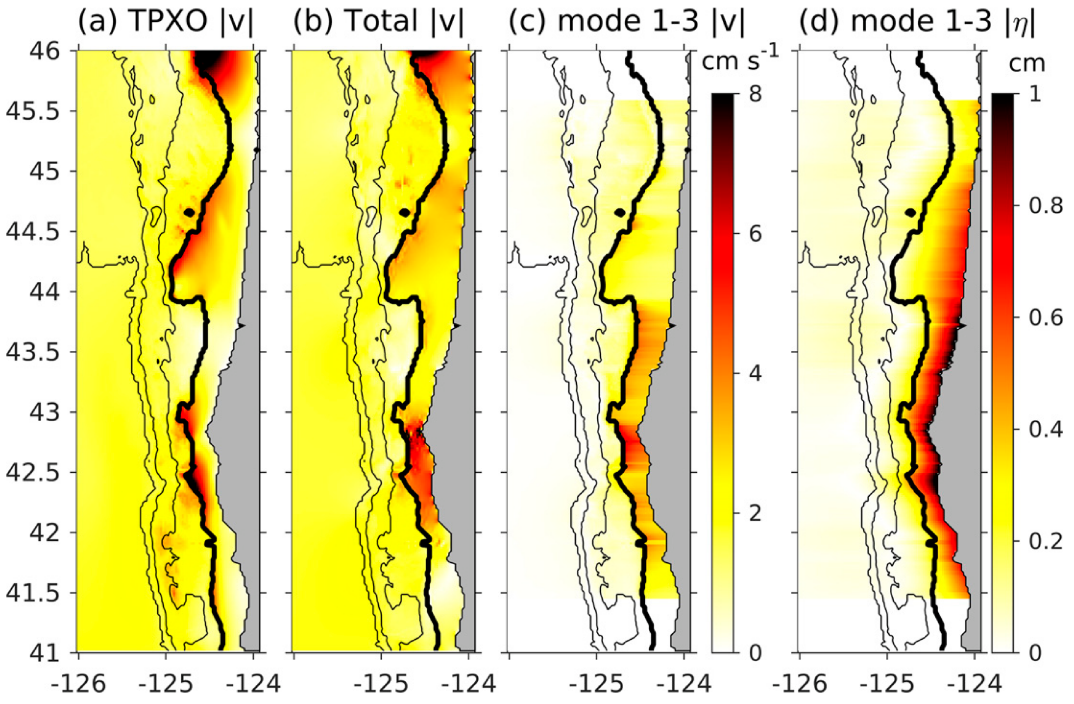


FIG. 10. The amplitude of the barotropic $K_1$ longshore velocity from (a) TPXO and (b) the MITgcm simulation. (c) The barotropic longshore velocity due to CTW modes 1–3 is enhanced from 42° to 44°N, and (d) the CTW surface displacement is approximately 1 cm. The depth-contour interval is 1 km, and a bold contour is plotted at 200 m. CTWs are not shown in the north and south sponge regions.

distance is treated like time. Modal forcing occurs when $\partial_x \mathbf{x}_n \neq 0$ because the modes change shape due to longshore variability in bathymetry or stratification. The modal evolution equation has an energy equation (18) that equates energy-flux divergence with topographic scattering (although we only examine generation).

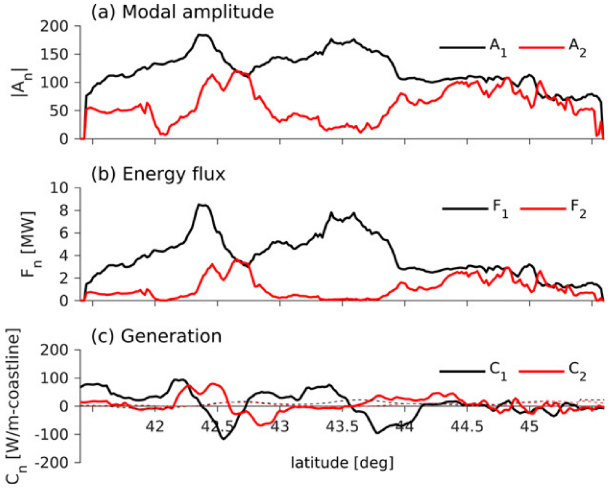


FIG. 11. Mode-1 and mode-2 (a) CTW amplitude, (b) energy flux, and (c) generation from the Oregon simulation. The difference between modal generation and flux divergence [$C_n - \nabla \cdot F_n$; dashed lines in (c)] can be interpreted as dissipation and has a significantly smaller magnitude than the generation terms [solid lines in (c)].

The modal theory (section 2) and the numerical method for determining CTW modes (section 3a) form a "toolbox" for precisely diagnosing CTW amplitudes, energy fluxes, and generation in numerical simulations. First, a set of numerically orthogonal CTW modes are obtained on the native simulation grid by solving (28). Then, modal amplitudes and energy fluxes are obtained by numerically computing (15) and (19). We quantified CTW generation by a longshore $K_1$ barotropic current flowing past a coastal bump. CTW generation is maximum when the bump's length of coastline matches the CTW wavelength, and increases quadratically with the amplitude of the bump, $W$. Both results are predicted from the modal evolution Eq. (16).

We also diagnosed CTWs on the Oregon coast. Amplitudes were large in the locations predicted by Osborne et al. (2014), although mode-1 and mode-2 CTW fluxes were only $\mathcal{O}(1–10)$ MW, which is much less than the 80 MW of $M_2$ internal-tide generation in this region (Osborne et al. 2011). Our results support the findings of Falahat and Nycander (2015), which indicate that trapped internal tides play a much lesser role in ocean mixing than freely propagating internal tides.

Widespread diagnosis of CTW generation in regional and global numerical simulations requires a way to deal with large-scale coastal curvature. This may require computing CTW modes on a grid that is nonnative to the simulation, which may compromise the numerical orthogonality of the modes. Precise orthogonality is critical because Kelvin wave

energy fluxes are often several orders of magnitude larger than mode-1 and mode-2 CTW energy fluxes, so even minor errors in the Kelvin wave amplitude may swamp CTW estimates. The radius of curvature must also be included in estimates of $\partial_x \mathbf{x}_n$.

An attractive alternative to analyzing regional or global simulations is to calculate modal amplitudes directly from the modal amplitude evolution equations (16). If the full fields $u$ and $p$ could be written as the sum of CTW modes, then the forcing terms in (16) could be computed using a modal matching technique. Wilkin and Chapman (1987) employed this method to estimate continental shelf wave scattering, but a short time later Middleton and Wright (1988) obtained erroneous solutions in some parameter regimes and concluded "there is some basic problem with either the assumed physics or the variety of mode matching solution techniques tried." We hypothesize that locally generated evanescent modes [the "residual" in (14)] must be included in the matching procedure, and these modes obey a separate set of evolution equations that are missing in the present analysis.

CTWs dissipate through intermodal scattering (Webster 1987), bottom drag (Brink 2006), and interactions with mean flows (Narayanan and Webster 1987). The modal amplitude equations (16) include scattering, but the energy transfer between two specific modes, $C_{mn}$, can only be obtained if $\mathbf{x}$ is expanded in (20) using (14), making total conversion $C_n = \sum_m C_{mn}$ (like scattering between vertical modes; Kelly et al. 2012). This expansion is hindered by the evanescent residual, which appears to mediate scattering. It may also be possible to extend the present toolbox to include orthogonal modes and/or modal amplitude equations that incorporate drag and mean-flow effects, although such an extension is nontrivial.

*Acknowledgments.* Kelly and Ogbuka were supported by the National Science Foundation Grant OCE-1635560. Ogbuka was also supported by the University of Minnesota Duluth Physics and Astronomy Department. This work benefited greatly from conversations with Ruth Musgrave, who also helped us setup the MITgcm simulations. Two anonymous reviewers improved the paper with insightful comments.

*Data availability statement.* The code for solving the eigenvalue problem, the MITgcm setup files, postprocessing scripts, and plot scripts are available at the Data Repository of University of Minnesota (DRUM; https://doi.org/10.13020/pt2w-sh61).

## REFERENCES

Allen, J. S., 1980: Models of wind-driven currents on the continental shelf. *Annu. Rev. Fluid Mech.*, **12**, 389–433, https://doi.org/10.1146/annurev.fl.12.010180.002133.

Antonov, J. I., and Coauthors, 2010: *Salinity*. Vol. 2, *World Ocean Atlas 2009*, NOAA Atlas NESDIS 69, 184 pp.

Brink, K. H., 1989: Energy conservation in coastal-trapped wave calculations. *J. Phys. Oceanogr.*, **19**, 1011–1016, https://doi.org/10.1175/1520-0485(1989)019<1011:ECICTW>2.0.CO;2.

——, 1991: Coastal-trapped waves and wind-driven currents over the continental shelf. *Annu. Rev. Fluid Mech.*, **23**, 389–412, https://doi.org/10.1146/annurev.fl.23.010191.002133.

——, 2006: Coastal-trapped waves with finite bottom friction. *Dyn. Atmos. Oceans*, **41**, 172–190, https://doi.org/10.1016/j.dynatmoce.2006.05.001.

——, and J. S. Allen, 1978: On the effect of bottom friction on barotropic motion over the continental shelf. *J. Phys. Oceanogr.*, **8**, 919–922, https://doi.org/10.1175/1520-0485(1978)008<0919:OTEOBF>2.0.CO;2.

Carrere, L., and Coauthors, 2021: Accuracy assessment of global internal tide models using satellite altimetry. *Ocean Sci.*, **17**, 147–180, https://doi.org/10.5194/os-17-147-2021.

Chapman, D. C., 1983: On the influence of stratification and continental shelf and slope topography on the dispersion of subinertial coastally trapped waves. *J. Phys. Oceanogr.*, **13**, 1641–1652, https://doi.org/10.1175/1520-0485(1983)013<1641:OTIOSA>2.0.CO;2.

Crawford, W. R., 1984: Energy flux and generation of diurnal shelf waves along Vancouver Island. *J. Phys. Oceanogr.*, **14**, 1600–1607, https://doi.org/10.1175/1520-0485(1984)014<1600:EFAGOD>2.0.CO;2.

Cushman-Roisin, B., and J.-M. Beckers, 2011: *Introduction to Geophysical Fluid Dynamics*. 2nd ed. Academic Press, 875 pp.

Dale, A., J. Huthnance, and T. Sherwin, 2001: Coastal-trapped waves and tides at near-inertial frequencies. *J. Phys. Oceanogr.*, **31**, 2958–2970, https://doi.org/10.1175/1520-0485(2001)031<2958:CTWATA>2.0.CO;2.

Egbert, G. D., 1997: Tidal data inversion: Interpolation and inference. *Prog. Oceanogr.*, **40**,53–80, https://doi.org/10.1016/S0079-6611(97)00023-2.

Falahat, S., and J. Nycander, 2015: On the generation of bottom-trapped internal tides. *J. Phys. Oceanogr.*, **45**, 526–545, https://doi.org/10.1175/JPO-D-14-0081.1.

Huthnance, J. M., 1975: On trapped waves over a continental shelf. *J. Fluid Mech.*, **69**, 689–704, https://doi.org/10.1017/S0022112075001632.

——, 1978: On coastal trapped waves: Analysis and numerical calculation by inverse iteration. *J. Phys. Oceanogr.*, **8**, 74–92, https://doi.org/10.1175/1520-0485(1978)008<0074:OCTWAA>2.0.CO;2.

Johnson, E. R., and J. T. Rodney, 2011: Spectral methods for coastal-trapped waves. *Cont. Shelf Res.*, **31**, 1481–1489, https://doi.org/10.1016/j.csr.2011.06.009.

Kelly, S. M., 2016: The vertical mode decomposition of surface and internal tides in the presence of a free surface and arbitrary topography. *J. Phys. Oceanogr.*, **46**, 3777–3788, https://doi.org/10.1175/JPO-D-16-0131.1.

——, 2019: Coastally generated near-inertial waves. *J. Phys. Oceanogr.*, **49**, 2979–2995, https://doi.org/10.1175/JPO-D-18-0148.1.

——, J. D. Nash, K. I. Martini, M. H. Alford, and E. Kunze, 2012: The cascade of tidal energy from low to high modes on a continental slope. *J. Phys. Oceanogr.*, **42**, 1217–1232, https://doi.org/10.1175/JPO-D-11-0231.1.

Lahaye, N., and S. G. Llewellyn Smith, 2020: Modal analysis of internal wave propagation and scattering over large-amplitude topography. *J. Phys. Oceanogr.*, **50**, 305–321, https://doi.org/10.1175/JPO-D-19-0005.1.

LeBlond, P. H., and L. A. Mysak, 1978: *Waves in the Ocean*. Elsevier, 602 pp.

Locarnini, R. A., A. V. Mishonov, J. I. Antonov, T. P. Boyer, H. E. Garcia, O. K. Baranova, M. M. Zweng, and D. R. Johnson, 2010: *Temperature*. Vol. 1, *World Ocean Atlas 2009*, NOAA Atlas NESDIS 68, 184 pp.

Marshall, J., A. Adcroft, C. Hill, L. Perelman, and C. Heisey, 1997: A finite-volume, incompressible Navier-Stokes model

for studies of the ocean on parallel computers. *J. Geophys. Res.*, **102**, 5753–5766, https://doi.org/10.1029/96JC02775.

Middleton, J. F., and D. G. Wright, 1988: Shelf wave scattering due to longshore jump in topography. *J. Phys. Oceanogr.*, **18**, 230–242, https://doi.org/10.1175/1520-0485(1988)018<0230:SWSDTL>2.0.CO;2.

Musgrave, R. C., 2019: Energy fluxes in coastal trapped waves. *J. Phys. Oceanogr.*, **49**, 3061–3068, https://doi.org/10.1175/JPO-D-18-0172.1.

——, 2022: The lifecycle of topographically-generated internal waves. *Ocean Mixing: Drivers, Mechanisms and Impacts*, M. Meredith and A. Naviera Garabato, Eds., Elsevier, 117–144, https://doi.org/10.1016/B978-0-12-821512-8.00013-X.

Mysak, L. A., 1980: Topographically trapped waves. *Annu. Rev. Fluid Mech.*, **12**, 45–76, https://doi.org/10.1146/annurev.fl.12.010180.000401.

Narayanan, S., and I. Webster, 1987: Coastally trapped waves in the presence of a barotropic shelf edge jet. *J. Geophys. Res.*, **92**, 9494–9502, https://doi.org/10.1029/JC092iC09p09494.

Osborne, J. J., A. L. Kurapov, G. D. Egbert, and P. M. Kosro, 2011: Spatial and temporal variability of the $M_2$ internal tide generation and propagation on the Oregon shelf. *J. Phys. Oceanogr.*, **41**, 2037–2062, https://doi.org/10.1175/JPO-D-11-02.1.

——, ——, ——, and ——, 2014: Intensified diurnal tides along the Oregon coast. *J. Phys. Oceanogr.*, **44**, 1689–1703, https://doi.org/10.1175/JPO-D-13-0247.1.

Parlett, B. N., 1980: *Classics in Applied Mathematics: The Symmetric Eigenvalue Problem*. SIAM, 391 pp.

Power, S. B., J. H. Middleton, and R. H. J. Grimshaw, 1989: Frictionally modified continental shelf waves and the subinertial response to wind and deep-sea forcing. *J. Phys. Oceanogr.*, **19**, 1486–1506, https://doi.org/10.1175/1520-0485(1989)019<1486:FMCSWA>2.0.CO;2.

Rainville, L., and R. Pinkel, 2006: Propagation of low-mode internal waves through the ocean. *J. Phys. Oceanogr.*, **36**, 1220–1236, https://doi.org/10.1175/JPO2889.1.

Rhines, P., 1970: Edge-, bottom-, and Rossby waves in a rotating stratified fluid. *Geophys. Fluid Dyn.*, **1**, 273–302, https://doi.org/10.1080/03091927009365776.

Robinson, A. R., 1964: Continental shelf waves and the response of sea level to weather systems. *J. Geophys. Res.*, **69**, 367–368, https://doi.org/10.1029/JZ069i002p00367.

Rodney, J. T., and E. R. Johnson, 2014: Meanders and eddies from topographic transformation of coastal-trapped waves. *J. Phys. Oceanogr.*, **44**, 1133–1150, https://doi.org/10.1175/JPO-D-12-0224.1.

Smith, W. H. F., and D. T. Sandwell, 1997: Global sea floor topography from satellite altimetry and ship depth soundings. *Science*, **277**, 1956–1962, https://doi.org/10.1126/science.277.5334.1956.

Stokes, G. G., 1846: Report on recent researches on hydrodynamics. British Association Rep. 1, 1–20.

Thomson, W., 1879: On gravitational oscillations of rotating water. *Proc. Roy. Soc. Edinburgh*, **10**, 92–100, https://doi.org/10.1017/S0370164600043467.

Wang, D.-P., and C. N. Mooers, 1976: Coastal-trapped waves in a continuously stratified ocean. *J. Phys. Oceanogr.*, **6**, 853–863, https://doi.org/10.1175/1520-0485(1976)006<0853:CTWIAC>2.0.CO;2.

Webster, I., 1985: Frictional continental shelf waves and the circulation response of a continental shelf to wind forcing. *J. Phys. Oceanogr.*, **15**, 855–864, https://doi.org/10.1175/1520-0485(1985)015<0855:FCSWAT>2.0.CO;2.

——, 1987: Scattering of coastally trapped waves by changes in continental shelf width. *J. Phys. Oceanogr.*, **17**, 928–937, https://doi.org/10.1175/1520-0485(1987)017<0928:SOCTWB>2.0.CO;2.

——, and D. Holland, 1987: A numerical method for solving the forced baroclinic coastal-trapped wave problem of general form. *J. Atmos. Oceanic Technol.*, **4**, 220–226, https://doi.org/10.1175/1520-0426(1987)004<0220:ANMFST>2.0.CO;2.

Wilkin, J. L., and D. C. Chapman, 1987: Scattering of continental shelf waves at a discontinuity in shelf width. *J. Phys. Oceanogr.*, **17**, 713–724, https://doi.org/10.1175/1520-0485(1987)017<0713:SOCSWA>2.0.CO;2.

——, and ——, 1990: Scattering of coastal-trapped waves by irregularities in coastline and topography. *J. Phys. Oceanogr.*, **20**, 396–421, https://doi.org/10.1175/1520-0485(1990)020<0396:SOCTWB>2.0.CO;2.

Yankovsky, A. E., and D. C. Chapman, 1995: Generation of mesoscale flows over the shelf and slope by shelf wave scattering in the presence of stable, sheared mean current. *J. Geophys. Res.*, **100**, 6725–6742, https://doi.org/10.1029/94JC03339.

——, and ——, 1996: Scattering of shelf waves by a spatially varying mean current. *J. Geophys. Res.*, **101**, 3479–3487, https://doi.org/10.1029/95JC02991.